INTERNATIONAL JOURNAL FOR NUMERICAL METHODS IN FLUIDS
Int. J. Numer. Meth. Fluids 2004; **44**:409–429 (DOI: 10.1002/fld.650)

Level-set based numerical simulation of a migrating and dissolving liquid drop in a cylindrical cavity

Edmondo Bassano*,†

MARS Center s.c.a.r.l., Via E. Gianturco 31, I-80146 Napoli, Italy

SUMMARY

In the present paper the dissolution of a binary liquid drop having a miscibility gap and migrating due to thermo-solutal capillary convection in a cylindrical cavity is studied numerically. The interest in studying this problem is twofold. From a side, in the absence of gravity, capillary migration is one of the main physical mechanisms to set into motion dispersed liquid phases and from the other side, phase equilibria of multi-component liquid systems, ubiquitous in applications, often exhibit a miscibility gap. The drop capillary migration is due to an imposed temperature gradient between the cavity top and bottom walls. The drop dissolution is due to the fact that initial composition and volume values, and thermal boundary conditions are only compatible with a final single phase equilibrium state.
In order to study the drop migration along the cavity and the coupling with dissolution, a previously developed planar two-dimensional code is extended to treat axis-symmetric geometries. The code is based on a finite volume formulation. A level-set technique is used for describing the dynamics of the interface separating the different phases and for mollifying the interface discontinuities between them. The level-set related tools of redistancing and off-interface extension are used to enhance code resolution in the critical interface region. Migration speeds and volume variations are determined for different drop radii. Copyright © 2004 John Wiley & Sons, Ltd.

KEY WORDS: level set; drop migration; miscibility gap; thermo-solutal capillary convection; cylindrical cavity

1. INTRODUCTION

In absence of gravity, capillary migration is one of the main physical mechanisms to set into motion dispersed liquid phases [1]. In several technological processes such phases are constituted by multi-component mixtures exhibiting a miscibility gap. Liquid mixtures constituted by the same components exhibit a miscibility gap if they coexist, in a given range of temperatures, in different phases at different compositions. A miscibility gap in the liquid phase is found in several different physical systems: metal alloys, mixtures of organic liquids, sulphides and silicates systems, glasses and liquid crystals, and many industrial applications are based on miscibility gap and related phenomena.‡ These two considerations promote the

*Correspondence to: E. Bassano, MARS Center s.c.a.r.l., Via E. Gianturco 31, I-80146 Napoli, Italy.
†E-mail: bassano@marscenter.it
‡MARS report "Welcome/FR-001", 2000.

Received 27 December 2002
Revised 5 August 2003

interest in studying the coupling between the migration and dissolution in multi-phase flows of multi-component liquid mixtures.

In the present paper the dissolution of a binary liquid drop having a miscibility gap and migrating due to thermo-solutal capillary convection in a cylindrical cavity is studied numerically.

The drop capillary migration is due to an imposed temperature gradient between the cavity top and bottom walls. The drop dissolution is due to initial composition and volume values of both phases and thermal boundary conditions which are only compatible with a final single phase equilibrium state. Local thermodynamic compositional equilibrium conditions at the drop inner and outer faces give rise to exchanges of total and partial mass between the phases through the interface that, in turn, determine the drop dimensions with varying the time and, in a large times scale, take the system towards the afore-mentioned global equilibrium state. As it will be shown, the evolution towards the final equilibrium is strongly affected by the drop initial radius.

Since capillary migration of drops is strongly affected, on Earth, by buoyancy due to both different densities of the mixture components and Boussinesq effects, the dissolution due to a miscibility gap and its influence on migration can be profitably studied in microgravity. In fact microgravity experiments on miscibility gap were conducted for more than two decades on almost every kind of microgravity platform (see footnote ‡). It must be noted that thermo-solutal gradients due to dissolution and latent heat of phase change can trigger, on Earth, strong buoyancy driven flows within the immersed and hosting phases also if they are in Plateau configuration, i.e. have similar densities. Solutal buoyancy effects can also affect the dissolution process in absence of migration f.i. in isothermal conditions.[§]

In order to study the drop migration along the cavity and the coupling with dissolution, a previously developed planar two-dimensional code has been extended to treat axis-symmetric geometries. The code is based on a finite volume formulation. A level-set technique is used for describing the dynamics of the interface separating the different phases and for mollifying the interface discontinuities between them. The level-set related tools of redistancing and off-interface extension are used to enhance code resolution in the critical interface region.

The simulations presented here are part of the research activities in both experimental and numerical field carried out at MARS Center for the preparation of a sounding rocket space experiment on the thermo-solutal capillary migration of dissolving drops to be hosted on-board the MAXUS 5 sounding rocket, in INEX-MAM facility, and flown in spring 2003.

The liquids selected for the sounding rocket experiment and used in numerical simulations are cyclohexane (C_6H_{12}) and methanol (CH_3OH). This couple of liquids has been selected because: (i) the components have nearly the same density; (ii) the liquids are transparent, allowing either the direct visualization of the drop migration and deformation either the use of optical diagnostics devices and (iii) their mixture has a critical temperature of 45.7°C, slightly larger than the ambient one and compatible with the INEX-MAM facility thermal requirements.

[§]MARS report: "Bread-Board Activities Test Report for Drop Dissolution and Migration Experiment", 2001.

2. NUMERICAL MODELLING UPGRADE

The present problem was already studied in a planar 2D geometry see for example in References [2–4]. In the present paper the previous code is extended to treat 2D axis-symmetric problems. This allows to correctly describe the physics of the migration process preserving the real topology, geometry and dynamics of the thermo-fluid dynamic field occurring during the space experiment.

The drop interface evolution is modelled by the level set technique, proposed by Osher and Sethian [5], in which the interface is represented by the zero level set of a scalar function defined within the computational domain. In order to maintain the level function and related quantities well-behaved during motion, this function is reinitialized as a distance function at each time step following Smereka *et al.* [6] and Peng *et al.* [7]. In order to model the interface dynamics more accurately than in previous works [2, 3], we extend the interface speed away from the interface, following the idea of Adalsteinsson and Sethian [8] and using the extension algorithm proposed by Peng *et al.* [7]. To this end we rewrite the level-set equation in a different form, more appropriate to interface extension, slightly different from the one-used in Reference [4]. We also use the extension algorithm to increase the accuracy of the momentum production terms. Since the level function needs to be defined only in a neighbourhood of the interface, the algorithms for redistancing and off-interface extension are localized as suggested in Reference [7] to reduce runtimes.

A third major modification to previous codes is a different formulation of the energy equation. In the past works the internal energy was used as dependent variable. Since the internal energy has a discontinuity at the interface due to the jump in the specific heat coefficient, its use was responsible for a poor accuracy in the calculation of the energy equation near the interface, which in turns gave temperature profiles with kinks not located on interface but slightly outside. It also gave a too small energy flux entering within the drop, a crowding of isotherms around it, and ultimately a tendency of the drop surface to become isotherm during migration. These problems, much more relevant in the axis-symmetric case than in the planar one, have been avoided by using as dependent variable the temperature, which is continuous at interface and has a discontinuity in the normal derivative only.

3. LEVEL-SET METHOD

In the level-set method for advancing fronts, the front, in our case the interface $\gamma(t)$, is represented at each instant of time t by the zero level set of a smooth scalar function ϕ. Let $x(t)$ be a representation of $\gamma(t)$ and $V_i(t) = \dot{x}(t)$ its velocity. Assume also that $x(0)$ is implicitly defined by the equation $\phi(x(0), 0) = 0$. The evolution equation for ϕ is described by the scalar equation of Hamilton–Jacoby type:

$$\phi_t + V_i \cdot \nabla\phi = \phi_t + V_{\text{in}}|\nabla\phi| = 0 \tag{1}$$

where ∇ is the nabla operator. In fact this equation states that, since at the initial time ϕ is constant along the curve γ moving in normal direction with speed $V_{\text{in}} = n \cdot V_i$, it will be constant there also at later times. In writing the second equality above, we have exploited the fact that the unit vector n normal to γ, ϕ being constant along it, can be written as $n = \nabla\phi/|\nabla\phi|$. Note

that the dynamics of γ is fully described by V_{in} only. In the following we assume that ϕ is positive outside γ and negative inside it so that n points outside γ.

4. LEVEL-SET RELATED TOOLS

In multiphase flows the level-set function is used not only for following the evolving front, but also for smoothing interface discontinuities, defining the dependent variables in the whole domain, expressing front related geometric quantities and interface production terms appearing in the coupling interface boundary conditions.

Following Smereka [9] and Sussman *et al*. [6], the generic dependent variable f is expressed in terms of the Heavyside step function $h(\phi)$ as $f=(f_{\text{ext}}-f_{\text{int}})h(\phi)+f_{\text{int}}$ and the interface source terms (of linear density f) are expressed as volume source terms, thanks to the equality

$$\int_\gamma f\,\mathrm{d}\gamma=\int_\Omega f|\nabla\phi|\delta(\phi)\,\mathrm{d}\Omega=\int_\Omega fn\cdot\nabla h\,\mathrm{d}\Omega \tag{2}$$

where $\delta(\phi)=\mathrm{d}h/\mathrm{d}\phi$ is the Dirac delta function, $\nabla h(\phi)=\nabla\phi\delta(\phi)$ and Ω a volume neighbourhood of the zero level set γ, i.e. a strip centred on γ.

In terms of the level-set function the trace k of the curvature tensor reads

$$\begin{aligned}k&=\nabla\cdot n=\nabla\cdot(\nabla\phi/|\nabla\phi|)=(\nabla^2\phi-\nabla|\nabla\phi|\cdot\nabla\phi/|\nabla\phi|)/|\nabla\phi|\\&=(\phi_{xx}\phi_y^2-2\phi_{xy}\phi_x\phi_y+\phi_{yy}\phi_x^2)/x(\phi_x^2+\phi_y^2)^{3/2}+\phi_x/x(\phi_x^2+\phi_y^2)^{1/2}\end{aligned} \tag{3}$$

and the immersed phase volume and centre of mass read

$$\text{vol}=2\pi\int(1-h_\varepsilon)x\,\mathrm{d}x\,\mathrm{d}y\qquad y_{\text{cm}}=2\pi\int(1-h_\varepsilon)xy\,\mathrm{d}x\,\mathrm{d}y/\text{vol} \tag{4}$$

where the integrals are extended on the whole computational domain.

The sign, Heavyside and Dirac functions are mollified as

$$\phi<-\varepsilon\quad \text{sgn}_\varepsilon(\phi)=-1\quad |\phi|\leqslant\varepsilon\quad \text{sgn}_\varepsilon(\phi)=\sin(\pi\phi/2\varepsilon)\quad \phi>\varepsilon\quad \text{sgn}_\varepsilon(\phi)=1 \tag{5}$$

$$h_\varepsilon(\phi)=[1+\text{sgn}_\varepsilon(\phi)]/2\quad \delta_\varepsilon(\phi)=\mathrm{d}h_\varepsilon/\mathrm{d}\phi \tag{6}$$

where $\varepsilon=m\Delta x$.

5. MODEL ASSUMPTIONS

Two liquid binary mixtures constituted by the same components exhibit a miscibility gap if they coexist, in a given range of temperatures, in two different phases having different compositions.

A binary liquid-phase decomposition into two phases at different composition can occur in the case in which the Gibbs free energy G diagram versus concentration, at constant temperature and pressure, is not convex, but has two local extrema. The (unique) line simultaneously

tangent at two points to the Gibbs free energy-mass fraction (c, G) diagram, individuates the two states coexisting at equilibrium. Their composition is the one of the tangency points and the partial Gibbs free energies, equal for both phases, are individuated by the intersections of the tangent with the vertical lines $c = 0$ and 1. The two phases at different composition can coexist since the condition of phase equilibrium is the equality of chemical potentials of the different phases that coincide with the partial Gibbs free energies of the components.

Varying the temperature the above couple of points defines in the (c, T) plane two branches of the so-called 'binodal' curve. In this plane a second curve called 'spinodal' (internal with respect to the binodal one) can also be drawn as the locus of points corresponding to the inflexion points of the $G(c)$ curve in the (c, G) plane. With increasing the temperature the tangent and inflexion points of the (c, G) plane collapse in the same minimum point (with vanishing second and third order derivatives). This points corresponds to the critical point of the (c, T) plane, in which the two branches of the binodal and spinodal curves converge with horizontal tangent. The region between binodal and spinodal lines is of metastable equilibrium and that between the branches of the spinodal line of unstable equilibrium.

The equilibrium methanol concentration c of each phase is reported as function of the temperature T in the equilibrium diagram in the (c, T) plane of Figure 1. The two branches of the equilibrium diagram, representing the equilibrium concentrations of the coexisting phases, match at the critical point where $\mathrm{d}c/\mathrm{d}T = \infty$ and the two phases merge in a single phase. It is supposed that at interface the concentrations are the equilibrium ones at the local temperature and that equilibrium always occurs at the binodal line of Figure 1.

Theoretical models for calculating the equilibrium curve are available and are particularly helpful for ideal solutions, but differences in atomic radius and bonding are responsible for possibly large discrepancies between real and ideal behaviour [10]. Having cyclohexane and methanol largely different molecules, their equilibrium phase diagram is given by points.

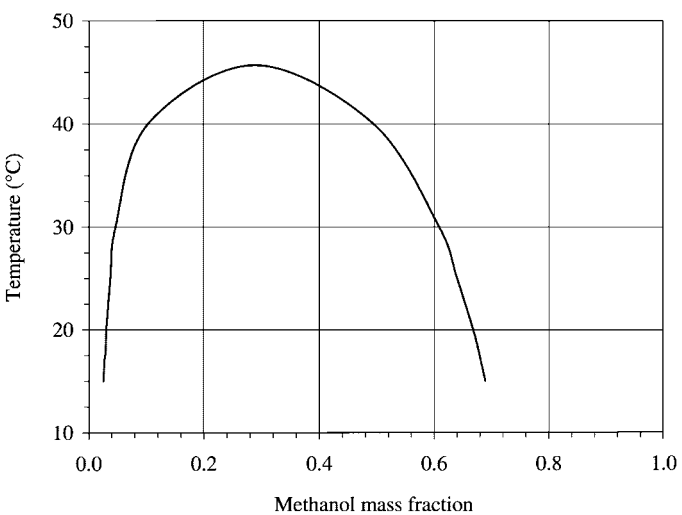

Figure 1. Cyclohexane-methanol phase diagram.

The surface phase is modelled as a pure interface. The surface tension σ is assumed to depend on temperature and equilibrium concentrations $\sigma = \sigma(T, c^+(T), c^-(T))$ where the superscript '+/−' indicates the external/internal side of the interface. At the critical point the different phases merge in a single phase and thus $\sigma_{\mathrm{cr}} = 0$. Since the equilibrium concentrations depend on the temperature one can assume $\sigma = \hat{\sigma}_{T0}(T - T_{\mathrm{cr}})$ [3]. According to experimental data $\hat{\sigma}_{T0} < 0$.

The motion being incompressible, the density ρ is constant in each phase. As cyclohexane and methanol have nearly the same density, the difference $\rho^+ - \rho^-$ is neglected.

6. INTERFACE BOUNDARY CONDITIONS

Mass conservation implies the continuity of the mass flow rate $\dot{m}$ through the interface

$$\dot{m} = \dot{m}^{\pm} = \{n \cdot \rho(V - V_i)\} \tag{7}$$

where $\{f\} = f^+ - f^-$ is the jump operator and the superscript '+' indicates the domain towards which n points.

Due to the hypothesis of phases of equal density, the normal component of the velocity $V_n = n \cdot V$ is continuous, but it differs from the interface normal speed

$$n \cdot V_i = V_{\mathrm{in}} = \left(n \cdot V - \frac{\dot{m}}{\rho} \right)^{\pm} \tag{8}$$

It is worth noting that this last equation holds also in the case of a discontinuous density.

In the present problem the mass flow rate through the interface $\dot{m}$ is obtained by imposing the conservation of the mass of each species at interface, i.e. the continuity of the normal total flux of species F

$$\{F\} = \dot{m}\{c\} - \{n \cdot \rho D \nabla c\} = 0 \tag{9}$$

and it is thus given by

$$\dot{m} = \{n \cdot \rho D \nabla c\}/\{c\} = \lfloor (\rho D c_n)^+ - (\rho D c_n)^- \rfloor / [c^+ - c^-] \tag{10}$$

The local mass fraction flux through the interface F is

$$F = F^{\pm} = \dot{m} c^{\pm} - (\rho D c_n)^{\pm} = \lfloor c^- (\rho D c_n)^+ - c^+ (\rho D c_n)^- \rfloor / [c^+ - c^-] \tag{11}$$

where the second equality (11) is obtained by substituting Equation (10) in Equation (11). The above formulae show that the same terms occurring in $\dot{m}$ appear also in F but are differently weighted. Thus these two fluxes may or may not have the same sign, depending on the actual values of the concentration and their normal derivatives at opposite sides of the interface.

As said before, the concentrations at interface sides $c^{\pm}$ are constrained to lie on the equilibrium curve at the local temperature. These concentration values, together with those of the concentration normal derivatives, in turn defines the entity of the interface dissolution cross-flow, species flux and interface normal velocity relative to the fluid, according to, respectively, Equations (10), (11) and (8). This last equation reads

$$V_{\mathrm{in}} = (n \cdot V - [(D c_n)^+ - (D c_n)^-]/[c^+ - c^-])^{\pm} \tag{12}$$

The flow being viscous, temperature and tangential velocity are assumed to be continuous at interface.

7. INITIAL AND EXTERNAL BOUNDARY CONDITIONS

The cavity containing the drop and the external liquid matrix is cylindrical. At the initial time the velocity is zero everywhere, the temperature is linearly stratified in axial direction, i.e. it is a linear function of the axial co-ordinate, the concentration is uniformly equal to one inside the drop $c_0^- = 1$, and to zero outside $c_0^+ = 0$. The drop is spherical with radius R and its centre is located on the symmetry axis at an ordinate y_0. The concentrations along the drop inner and outer faces are fixed by the local temperature according to the equilibrium curve. The initial time discontinuity between the inner (outer) drop surface and the interior (exterior) is regularized by a complementary error function profile decaying in few cells $c = c_0^{\pm} + (c^{\pm} - c_0^{\pm})\,\mathrm{erfc}\,(\pm k\phi/\varepsilon)$ where $k = 2.5$, $\varepsilon = 5\Delta x$.

On the cavity walls the velocity vanishes. Top and bottom walls are held at constant different temperatures, T_t and T_b respectively, with $T_t > T_b$, the lateral wall is adiabatic, i.e. $T_n = 0$ at the lateral boundary. There is no diffusion of species through the cavity walls, i.e. $c_n = 0$ all along the cavity boundary. The boundary and initial conditions are sketched in Figure 2.

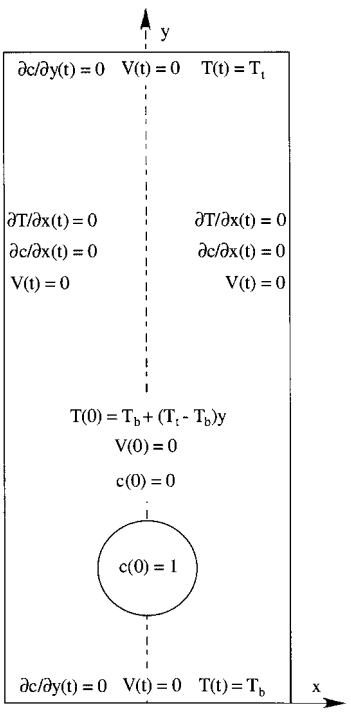

Figure 2. Initial and boundary conditions.

8. MOTION EQUATIONS

In the following p is the average normal stress, μ the dynamic viscosity, v the kinematic viscosity, c_s the specific heat coefficient, α the thermal diffusivity, λ the thermal conductivity and D the diffusion coefficient.

The motion equations are formulated in a standard imbedded boundary approach by defining the dependent variables in the whole domain, as shown in Section 2. The transport properties, specific heat and density are constant in each phase. The non-dimensional motion equations for the present problem can be written as

$$\nabla \cdot V = 0 \tag{13}$$

$$V_t + \nabla p = \nabla \cdot \lfloor \mu(\nabla V + (\nabla V)^{\mathrm{T}})/Re - VV \rfloor + [(T - T_{\mathrm{cr}} - We_{\mathrm{T}}/We)kn - \nabla_{\mathrm{s}} T](n \cdot \nabla h)/We_{\mathrm{T}} \tag{14}$$

$$T_t + \nabla \cdot (TV) - \nabla \cdot (\lambda \nabla T)/c_{\mathrm{s}} Ma = 0 \tag{15}$$

$$c_t + \nabla \cdot [V - D\nabla c/Re\,Sc] = 0 \tag{16}$$

$$\phi_t + V_{\mathrm{in}} |\nabla \phi| = 0 \tag{17}$$

where the superscript 'T' indicates transposition, $\nabla_{\mathrm{s}} = \nabla - n\partial/\partial n$ is the surface nabla operator, k the interface curvature and the non-dimensional density is omitted being uniformly equal to one. The non-dimensional characteristic Schmidt Sc, Reynolds Re, Marangoni Ma, Weber We and thermo-solutal Weber We_{T} numbers are given by

$$Sc = v_{\mathrm{r}}/D_{\mathrm{r}} \quad Re = RV_{\mathrm{r}}/v_{\mathrm{r}} \quad Ma = RV_{\mathrm{r}}/\alpha_{\mathrm{r}} \quad We = V_{\mathrm{r}}^2 \rho_{\mathrm{r}} R/\hat{\sigma}_0 \quad We_{\mathrm{T}} = V_{\mathrm{r}}^2 \rho_{\mathrm{r}} R/|\hat{\sigma}_{T0}| T_{\mathrm{r}} \tag{18}$$

As reference quantities, we choose

$$V_{\mathrm{r}} = |\hat{\sigma}_{T0}| T_{\mathrm{r}}/\mu_{\mathrm{r}} \quad L_{\mathrm{r}} = R \quad t_{\mathrm{r}} = R/V_{\mathrm{r}} \quad p_{\mathrm{r}} = \rho_{\mathrm{r}} V_{\mathrm{r}}^2 \quad T_{\mathrm{r}} = (T_{\mathrm{t}} - T_{\mathrm{b}})R/H \tag{19}$$

while c_{sr}, D_{r}, λ_{r}, μ_{r} and ρ_{r} are those of the external fluid. One has $We_{\mathrm{T}} = Re$. Energy dissipation due to momentum diffusion is neglected.

Since the latent heat of phase change is small for the considered system the corresponding term in the energy equation (15) is neglected. This amounts to have a continuous diffusive heat flux. This approximation will be removed in a forthcoming paper.

9. NUMERICAL IMPLEMENTATION

This section is devoted to numerical implementation. The algorithm for motion equations is detailed in the first sub-section. Level-set related tools of redistancing and off-interface extension are treated in the following sub-sections. All the algorithms of this section are localized as in Reference [7]. A flow diagram of the steps taken during each iteration is shown in Figure 3.

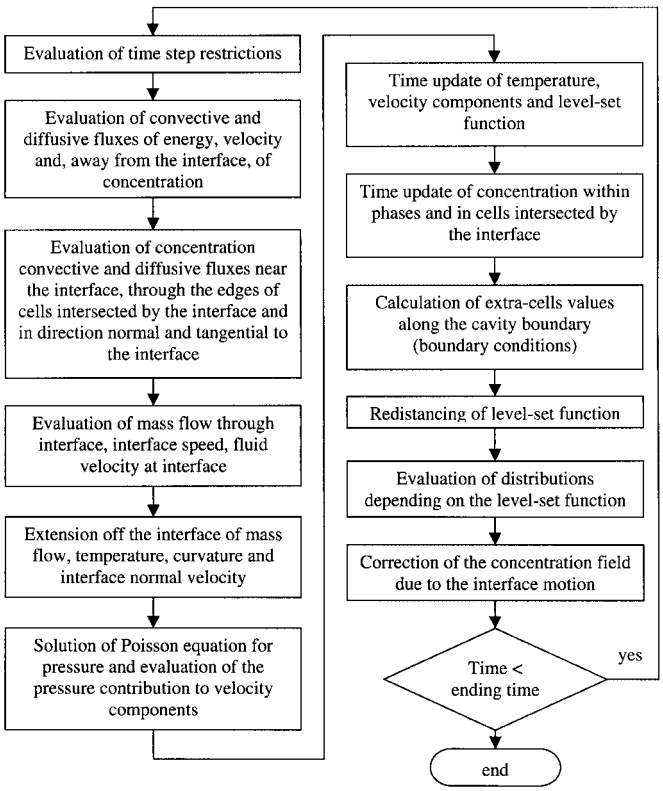

Figure 3. Flow diagram summarizing the steps taken in the numerical algorithm.

9.1. Motion equations algorithm

The system of motion equations in conservation form was solved by a finite volume approach on a staggered grid. The fluxes were evaluated by essentially non-oscillatory (ENO) upwind biased three points formulae, diffusive fluxes with second order centred formulae. The ordinary Chorin–Temam projection method was used to determine the indivergent velocity vector field. The pressure Poisson equation was solved with a successive over relaxations (SOR) algorithm. The space semi-discretized equations were advanced in time with a first-order Euler explicit time stepping.

The level-set function derivatives occurring in the expression of k in Equation (3) are calculated with second-order centred formulae.

Since the simultaneous jump singularities of concentration and concentration normal derivative, referred to in Section 3, cannot be easily mollified while retaining the necessary accuracy of the cross-flow rate, a scheme for the species equation allowing sharp jumps and having subcell resolution was conceived in References [2–4] and detailed in Reference [4]. Since the species equation numerics are already discussed there they are not readdressed here. The same algorithm is used here with only minor modifications needed to take into account the axial symmetry.

9.2. Redistancing algorithm

Functions d such that $|\nabla d| = 1$ everywhere are called distance functions. Accuracy requires that the level-set function ϕ has this property. Even if one initializes ϕ as a distance function, ϕ can smear out or steep. To ensure that ϕ remains a distance function at least near the interface, Sussman *et al.* [6] proposed to reinitialize ϕ at each step by solving the hyperbolic equation to steady state

$$d_\tau = \operatorname{sgn}(\phi)(1 - |\nabla d|) \qquad d(x,0) = \phi(x,t) \tag{20}$$

where τ plays the role of a parameter. The redistancing problem is of Hamilton–Jacoby type. A semi-discretized approach is used to solve Equations (20). For the space discretization the general Godunov numerical flux function proposed by Osher and Shu [11] is used, calculated as shown in Jiang and Peng [12].

The fifth order weighted essentially non-oscillatory (WENO) scheme proposed by Jiang and Shu [13] is used for the calculation of the derivatives. Third order total variation diminishing (TVD) Runge–Kutta algorithm of Gottlieb and Shu [14] is used for time integration.

In order to ensure the necessary accuracy of the curvature and to enhance volume conservation during redistancing, the sign function is mollified as proposed in Peng *et al.* [7]. This prevents errors due to node crossing by the zero level set during reinitialization and allows adapting stencil support according to the local value of the gradient modulus.

9.3. Off-interface extension algorithm

The off-interface extension of a generic quantity f is performed by solving the following Hamilton–Jacoby equation

$$f_\tau + \operatorname{sign}(\phi)\, n \cdot \nabla f = 0 \qquad f(x,0) = f(x,t) \tag{21}$$

until steady state. At the steady state the function f is constant in the direction of n (in which ϕ varies)

$$n \cdot \nabla f = 0 \qquad \nabla\phi \cdot \nabla f = 0 \tag{22}$$

and is equal to the value it has on the zero level set. Since extending f off the interface amounts to zeroing its normal derivative, the gradient of f calculated after the extension retains its tangential contribution only.

If a locally constant function f is multiplied by a (symmetrically) mollified Dirac function the extrema of the product function are all located on the zero level set and coincide with $f(0)\,\delta_\varepsilon(0)$. If f, instead, is locally strictly monotone, the extrema of the product function do not fall on the zero level set and differ from $f(0)\,\delta_\varepsilon(0)$. These properties of extended functions are exploited for the evaluation of the normal and tangential momentum production terms

$$((T - T_{\mathrm{cr}})/We_{\mathrm{T}} - 1/We)\, k|\nabla\phi|\,\delta(\phi)\, n \qquad -(\nabla_{\mathrm{s}} T/We_{\mathrm{T}})|\nabla\phi|\,\delta(\phi) \tag{23}$$

According to above observations temperature (and curvature) extension give a more accurate evaluation of the first term. The tangential gradient in Equation (23) is calculated as $\nabla_{\mathrm{s}} T = (I - nn)\nabla T = \nabla T - n\partial T/\partial n$. Here temperature extension makes vanishing the normal components of the temperature gradient, that it is important to note are discontinuous, leaving only the tangential contribution which is instead continuous.

Following Peng *et al.* [7], also the interface velocity in Equation (1) is extended off the interface. Numerical experiments revealed that the extending procedure greatly enhances the simulation accuracy avoiding the appearance of spurious vortical structures within the interface strip and allowing for a far better resolution of the curvature.

The integration of Equation (21) is performed using formulas similar to those of the previous sub-section.

10. RESULTS

The INEX-MAM cell is 3 cm wide, 3 cm deep and 6 cm long in the temperature gradient direction. The 2D axis-symmetric simulation domain corresponds to the right half of an axial planar section of a cylindrical cavity having a radius of 3 cm and a height of 6 cm.

At the initial time $t = 0$ s, the centre of drop is located on the symmetry axis. The drop centre distance from the lower wall is 1 cm. We considered three different drop radii: $R = 0.25, 0.5$ and 0.75 cm. The cold temperature T_b is set to 15°C, the hot one, T_t, to 55°C. Accordingly the imposed temperature gradient is 6.66°C/cm. Initially the temperature profile is linearly stratified between the upper and lower wall temperatures, the drop is of pure methanol, the surrounding matrix of pure cyclohexane, both phases are quiescent.

The properties of the fluids used in the simulations are reported in Table I. Non-dimensional characteristic numbers depending only on fluid properties, Prandtl and Schmidt numbers are also reported in the same table. Internal and external Reynolds and Marangoni numbers, depending on R, are listed in Table II.

Table I. Properties of cyclohexane and methanol.

	Cyclohex.		Methanol
ρ	0.779		0.779
μ	0.980 e − 2		0.790 e − 2
ν	1.258 e − 2		1.014 e − 2
λ	1.248 e 4		2.020 e 4
c_s	1.859 e 7		2.533 e 7
D	1.000 e − 5		1.000 e − 5
σ_T		−0.01	
Pr	14.60		9.904
Sc	1258		1014

Table II. External and internal Reynolds and Marangoni numbers based on the properties of Table I for three radii.

R	Re_{ext}	Ma_{ext}	Re_{int}	Ma_{int}
0.25	34	493	42	415
0.5	135	1974	168	1661
0.75	304	4441	377	3737

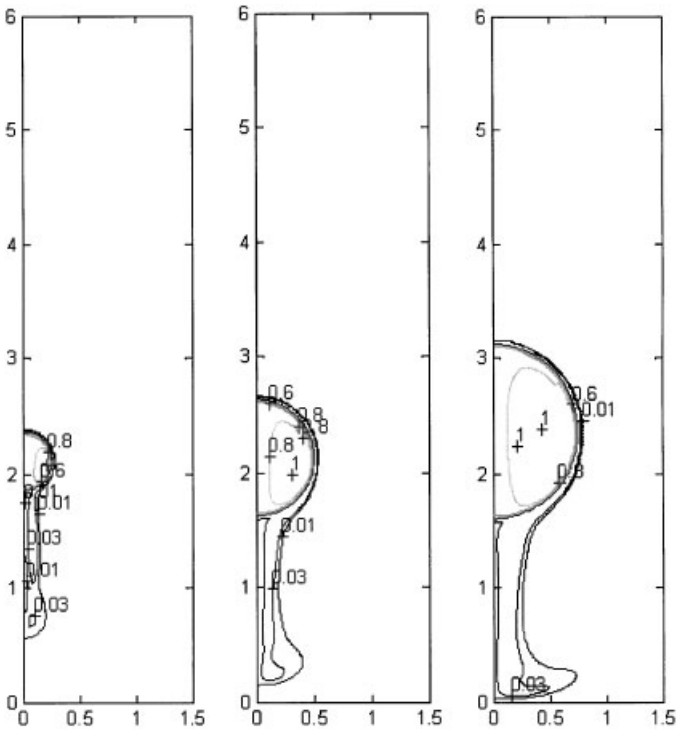

Figure 4. Concentration isolines at start-up, $t = 14.7$ s for $R = 0.25$ cm, $t = 10.3$ s for $R = 0.5, 0.75$ cm.

The computational grid in the axial semi-plane is composed of 60×240 square cells, 80×320 square cells are used for the smaller drop. Preliminary tests showed that used grids are sufficiently refined for large and medium drops, while grid refinement is probably required for the small drop, but has not been pursued here due to the large computational times required. In all simulations we use $m = \frac{1}{2}$ in Equations (4) and $m = 3$ in Equations (5) and (6).

During the initial start-up phase of the drop motion, which is similar for all cases, both internal and external liquids are dragged along the drop surface by the interface tension gradient. The internal fluid dragged along the interface is warmer than the drop bulk, which is wrapped and tends to stay cold due to the large internal Peclet number. When the inner surface driven flow reaches the rear pole, it rises along the symmetry axis, reaches the front region and then flows back, creating a ring vortex inside the drop as evidenced by the concentration isolines of Figure 4(a)–(c) (the radius increases from left to right). At the same time the external fluid dragged along the external side of the drop creates a warm wake behind the drop, entraining the cold bottom region of the cavity Figure 5(a)–(c) (the radius increases from left to right).

After a sudden acceleration, due to the rise of surface tension forces, the drop velocity decreases, since the isotherms wrap around the drop, whose surface tends to become isotherm. The drop vertical velocity versus time is plotted in Figure 6. After the initial deceleration

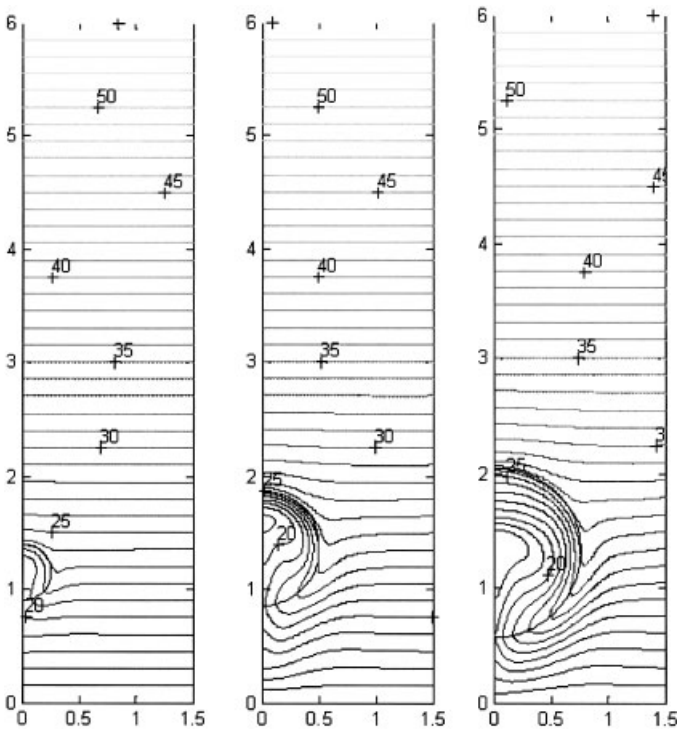

Figure 5. Temperature isolines at start-up, $t = 1.47$ s for $R = 0.25$ cm, $t = 2.94$ s for $R = 0.5, 0.75$ cm.

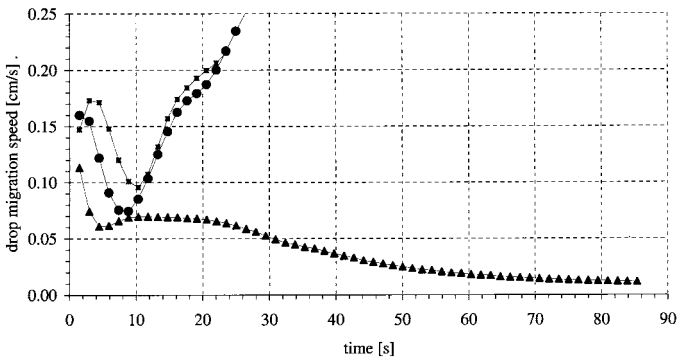

Figure 6. Drop vertical velocity versus time. Triangles $R = 0.25$ cm, circles $R = 0.5$ cm and squares $R = 0.75$ cm.

occurring whatever is the radius during the first 10 s, the medium and large drops start newly to accelerate and their speed increases until the drop stops at the hot wall of the cavity. Particularly, the medium drop reaches a larger velocity having a longer path to migrate before touching the hot wall. On the contrary, for the small drop, the initial deceleration creates a wave in the front of the drop that destroys the stratified linear profile and determines a drop

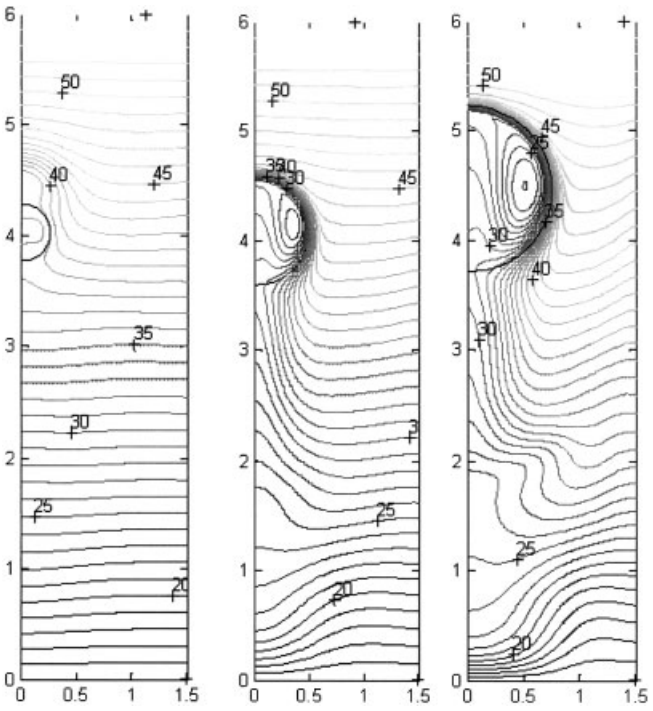

Figure 7. Wall temperature gradient perturbations for the three radii of Table II.

slowing, as shown by the temperature distribution in Figure 7(a). This behaviour is due to the fact that the small drop cools more quickly than larger drops and its surface becomes nearly isotherm. At later times the temperature ceases to decrease monotonically along the surface of the small drop and the interface tension maximum ceases to be located on the symmetry axis. This leads to the inversion of the direction of the interface tension near the interface fore pole. The inverted flow region grows and gives rise to a second (counter-rotating) vortex within drop. The outer fluid in the front of the drop is pushed up towards the hot wall and the inner fluid is pushed back down towards the drop centre, as indicated by the isotherms of Figure 7(a). The occurrence of the reverse flow in front of the smaller drop has been observed both on differently refined grids and with different stencils for the convective terms so it does not seem to be a numerical artifact.

As shown in Figure 7(a)–(c) (the radius increases from left to right), the stratified temperature profile near the lateral wall is: left almost unperturbed by the small drop, slightly perturbed by the medium drop, highly distorted by capillary convection around the largest drop. Therefore, the largest drop migrates subjected to a non-uniform temperature gradient.

During its ascent every drop warms up, as shown in Figure 7(a)–(c). The smaller is the radius the warmer is the drop and the faster is reduction of the thermal wake behind it.

No noticeable drop shrinking can be observed during the drops ascent as shown in Figure 8, where the drop shapes are reported at constant intervals of time from bottom to top of each picture.

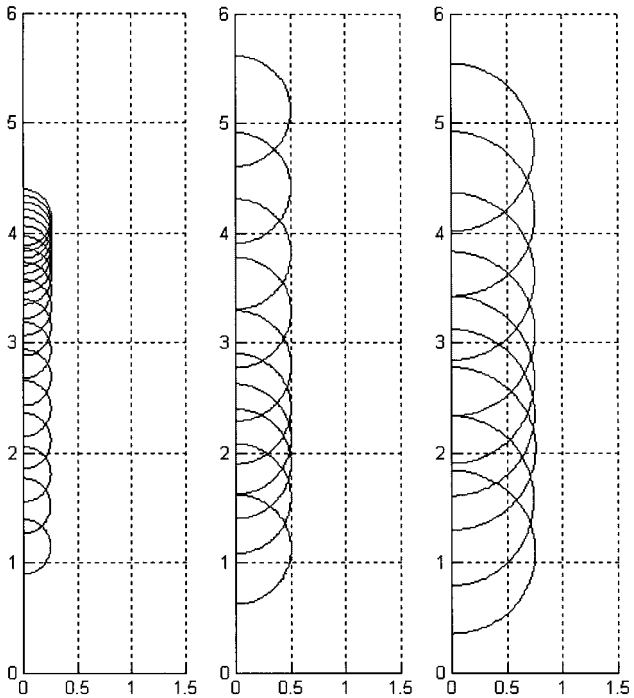

Figure 8. Drop shapes during the ascent. Initial time $t = 1.47$ s, $\Delta t = 4.41$ s for $R = 0.25$ cm, $\Delta t = 1.47$ s for $R = 0.5, 0.75$ cm.

Besides the thermal Marangoni convection, the concentration field is also affected by dissolution.

According to the initial conditions and binodal curve, the concentration decreases going from the inner phase to the inner surface of the drop and still decreases going from the outer surface towards the external phase. The internal vortical flow that establishes after the start-up is characterized by concentration values lower than those of the ring vortex core both near the drop surface and along the axis. Obviously this is due to the fact that the low concentration fluid had been convected along the interface, where the concentration was fixed by the binodal curve, as shown in Figure 4(a)–(c). The outer flow drags a more concentrated fluid in the wake. In the first part of the drop rise, the concentration field follows the qualitative evolution of the thermal field, as shown in Figures 4 and 5, even if the diffusion of matter is sensibly lower than that of energy, Schmidt numbers being larger than Prandtl numbers. It must be noted that the less concentrated fluid rising along the drop axis is convected downward by the vortex ring before reaching the fore pole and the interface.

After a complete turn of the fluid along the drop surface and axis, the inner low (outer high) concentration regions become larger due to the depletion (enrichment) of the fluid along the interface, as one can see e.g. in Figure 9.

As shown in the same figure, the mass fraction of the external phase changes slightly and in the wake only, due to the very low diffusion coefficient and to the low values of the concentration along the left branch of the binodal curve of Figure 1. The mass fraction

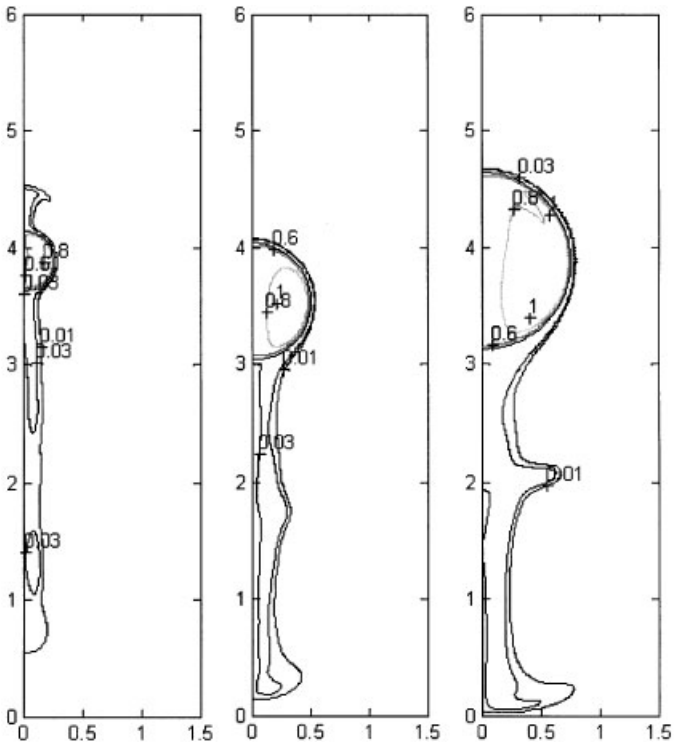

Figure 9. Concentration isolines during ascent. $t = 58.8$ s for $R = 0.25$ cm, $t = 20.6$ s for $R = 0.5, 0.75$ cm.

variations are instead appreciable within the drop. Here the concentration changes from the initial unit value to values lower than 0.7 at the drop inner surface. The unit concentration persists in a region near the ring vortex core.

Differently from the case of the mass flow through the interface discussed below, no conclusions on the sign of the concentration flux, given by Equation (11), can be drawn a priori, since the two terms in the r.h.s. are about the same order of magnitude at the initial time. The positiveness of the concentration flux through the interface during migration is revealed by the already noted increase of the concentration outside the drop and in the wake. However, it is important to underline that, according to Equations (10) and (11), dissolution can also occur while the volume increases, i.e. partial mass flux can be positive even if the mass flux is negative.

In the present problem the volume flow through the drop interface is proportional to the mass flow, the phases being isodense and the flow incompressible. The local mass flow through the interface $\dot{m}$, according to Equation (10), is proportional to the difference of the concentration normal derivatives and inversely proportional to the concentration jump, which depends on the local temperature and goes to zero at the critical point. Thus, according to Figure 1, the denominator of (10) is always negative, the concentration of methanol being larger in the inner phase. An increase of temperature can cause an increase of the intensity

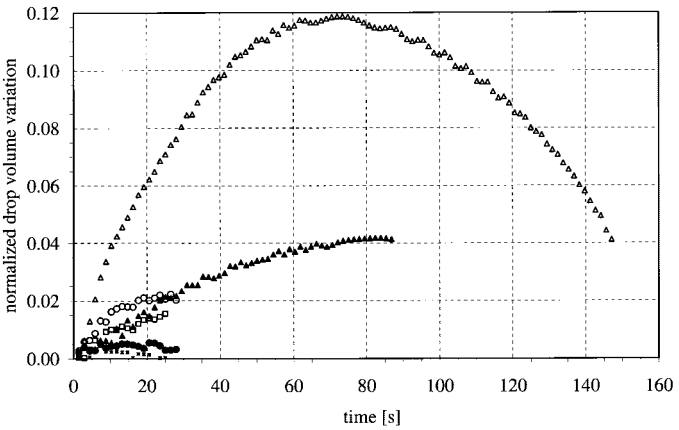

Figure 10. Normalized drop volume variation defined as $(\mathrm{vol}(t)/\mathrm{vol}(0) - 1)$, where $\mathrm{vol}(0)$ is the initial drop volume. Triangles $R = 0.25$ cm, circles $R = 0.5$ cm and squares $R = 0.75$ cm. Empty symbols correspond both Marangoni migration and dissolution. Filled symbols to migration without dissolution.

of $\dot{m}$ but not a sign change. At initial time the concentration normal derivatives are both negative. The initial conditions and the binodal curve make the inner normal derivative, in modulus, fairly larger than the external one, of about an order of magnitude. This leads to the conclusion that at least for short times the drop volume shall increase. In absence of convection, volume variation should occur in times of the order of the diffusive characteristic time R^2/D and then the volume should increase for quite long times.

The drop relative volume variation $\mathrm{vol}/\mathrm{vol}(0) - 1$ is plotted versus time in Figure 10, where the empty symbols refer to dissolution and the filled symbols refer to absence of dissolution. The volume variation in the second case (only Marangoni migration) should be zero in all cases. A value of about 4% indicates that a grid refinement is still necessary for small drops. Medium and large drops grow slightly and slowly while smaller drops grow more and faster.

Nevertheless the comparison of corresponding curves shows that dissolution is responsible of an increase of dimensions. At start-up the drop cold core is wrapped by the warmer fluid dragged by interface tension along its surface. Since the energy exchange by heat between the rising drop and the surrounding phase is very small, the drop tends to stay cold. Accordingly, the external isotherms encountered by the drop during the ascent slightly penetrate within the drop and fold over it. The drop pushes the isotherms up and constrains them in a narrow thermal boundary layer, surrounding the drop and having a steep normal temperature gradient, as shown in Figures 5 and 7.

Therefore the temperature on the drop surface does not change appreciably during the rise and remains lower than the one corresponding to the unperturbed stratified profile at the actual height. Correspondingly the concentration jump across the interface $(c^+ - c^-)$, appearing in the denominator of Equation (10), neither goes to zero nor decreases appreciably and the mass flow rate $\dot{m}$ remains bounded also in the upper part of the cavity, where the unperturbed temperature is higher than the critical one.

In Figures 11–14 are plotted the concentration profiles in planes passing through the cell centre nearest to the drop centre of mass and inclined at 90°, 0°, −90° w.r.t. the horizontal

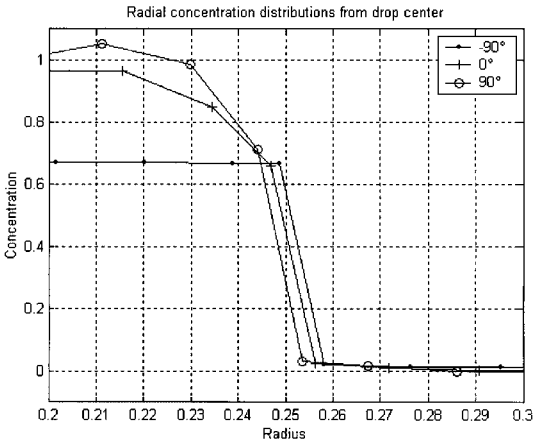

Figure 11. Radial concentration distribution for $R = 0.25$ cm along three different radial directions at $t = 1.47$ s.

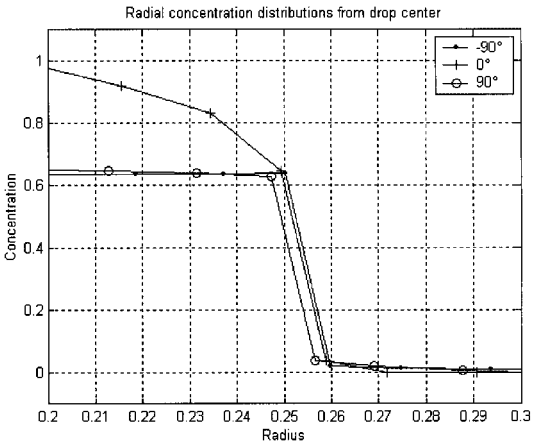

Figure 12. Radial concentration distribution for $R = 0.25$ cm along three different radial directions at $t = 23.5$ s.

for the small drop at different increasing times. The plots show a neighbourhood of the interface. Here the displacement of the interface position in different sections is mainly due to the fact that intersection planes are not exactly barycentric. The remarkable differences in the concentration profiles within the drop are due to the fact that the $\pm 90°$ profiles lie along the axis, where the low concentration fluid coming from the drop inner surface rises, pushed by the inner Marangoni flow, while the 0° profile cuts the high concentration region of the ring vortex core. The difference of the outer concentration profiles is due to the fact that the 90° and 0° profiles extend in unperturbed regions while the $-90°$ profile extends in the wake. The line connecting the inner and outer concentration is added by the visualization software but it must not be considered as part of the profile since in our calculation the concentration

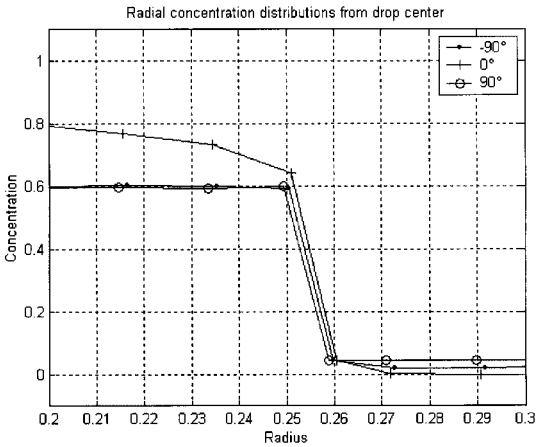

Figure 13. Radial concentration distribution for $R = 0.25$ cm along three different radial directions at $t = 50$ s.

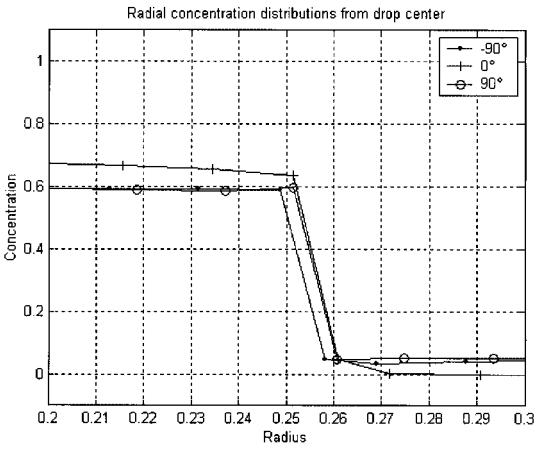

Figure 14. Radial concentration distribution for $R = 0.25$ cm along three different radial directions at $t = 72.1$ s.

jump is sharp. The normal derivatives (coinciding with the radial derivatives since the drop is nearly spherical) are given by the profile slopes at the sides of the interface represented by the almost vertical segment. In the present case Equations (10) and (11) can be written, respectively, as

$$\dot{m} = \rho D(-|c_n^-| + |c_n^+|)/|c^- - c^+| \quad F = \rho D(-c^+|c_n^-| + c^-|c_n^+|)/|c^- - c^+| \tag{24}$$

where the normal co-ordinate n increases like the radial one. By comparing the inner and outer slopes at the interface, one deduces that the mass flow through the interface is large and negative for the horizontal profile. Since the same happens also for a large part of the radial profiles (not displayed in the figures), the global exiting mass flux (the integral of $\dot{m}$

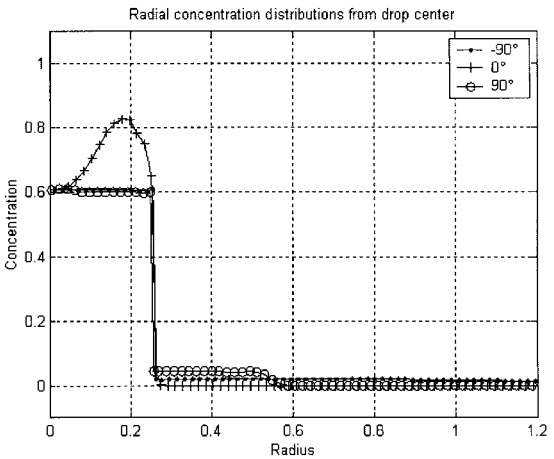

Figure 15. Radial concentration distribution for $R = 0.25$ cm along three different radial directions at $t = 16.2$ s.

along the interface) is negative and the drop increases in volume. At later times the volume growth first decreases and then stops as shown by the curve in Figure 9 and by the profiles of Figures 11–14. At still larger times, simulated for the small drop only, the drop volume decreases as expected.

Since $c^- \gg c^+$ and the inner normal derivative is small at both poles for the small drop, according to Equation (24), the methanol flux is positive at poles and a methanol plume develops there as shown in Figure 15. For medium and large drops the methanol plume is instead present only at the rear pole.

In the case of small drop, even if energy diffusion is quite limited, it is nevertheless sufficient to reduce drop temperature, due to the reduced drop dimensions. The migration of the small drop is also slower and the drop has a larger time to adapt itself to the external conditions. The increase of the drop surface temperature, through the concentration jump at the interface, also contributes to a volume variation faster than that of bigger drops. Finally it must be considered that a given volume variation, when normalized w.r.t. the initial volume, increases with decreasing the initial dimensions.

11. CONCLUSIONS

In the present paper the thermo-solutal-capillary multiphase flow of a binary mixture exhibiting a miscibility gap is numerically investigated. A fixed grid level-set based algorithm is used in order to follow the drop motion allowing it to deform freely. A high-order redistancing algorithm is used to enhance the accuracy of the level-set approach. In order to obtain an accurate evaluation of the volume production terms coming from the level-set formulation of the boundary conditions between the different phases, an off-interface extension algorithm is used for the correct location of distributions, mollification, and filtering of the quantities related to such terms. It is noteworthy that in the present paper both tangential stresses and mass flow

through the interface are considered. A previously developed and tested algorithm [4], able to resolving the concentration interface singularity and evaluating the interface cross-flow, is used for the mass fraction equation. Numerical simulations show that the concentration singularity is quite well resolved also in this axis-symmetric case. The code models the transient start-up phase and the following migration, and allows to evaluate the effects on migration of external walls, different drop dimensions and dissolution. The thermo-fluid dynamic field evolution is discussed on the basis of the obtained numerical results.

REFERENCES

1. Shankar Subramanian R, Balasubramaniam R. In *The Motion of Bubbles and Drops in Reduced Gravity*. Cambridge University Press: Cambridge, 2001.
2. Bassano E, Castagnolo D, Albano F. Thermocapillary two-phase flow of a binary mixture drop exhibiting a miscibility gap. IAF-01-J.4.09, *52nd IAC Congress*, Tolouse, France, 1–5 Oct. 2001.
3. Bassano E, Castagnolo D. Marangoni migration of a methanol drop in cyclohexane matrix in a closed cavity. *Microgravity Science and Technology* 2003, accepted for publication.
4. Bassano E. Numerical simulation of thermo-solutal-capillary migration of a dissolving drop in a cavity. *International Journal for Numerical Methods in Fluids* 2003, accepted for publication.
5. Osher S, Sethian J. Fronts propagating with curvature-dependent speed: algorithms based on Hamilton-Jacobi formulation. *Journal of Computational Physics* 1988; **79**:12–49.
6. Sussman M, Smereka P, Osher S. A level set approach for computing solutions to incompressible two-phase flow. *Journal of Computational Physics* 1994; **114**:146–159.
7. Peng D, Merriman B, Osher S, Zhao H, Kang M. A PDE-Based fast local level set method. *Journal of Computational Physics* 1999; **155**:410–438.
8. Adalsteinsson. D, Sethian, JA. The fast construction of extension velocities in level set methods. *Journal of Computational Physics* 1999; **148**:2–22.
9. Smereka P. Level set methods for two-fluid flows. INRIA short course lecture notes.
10. Ratke L. In *Immiscible Liquid metals and organics*. DGM Informationsgesellshaft, 1993.
11. Predel B, Ratke L, Fredriksson H. In Walter H.U. (ed.). *Fluid Science and Material Science in Space*. Springer: Berlin, 1987.
12. Osher S, Shu CW. High-order essentially nonoscillatory schemes for Hamilton–Jacobi equations. *SIAM Journal of Numerical Analysis* 1991; **28**:907–922.
13. Jiang G-S, Peng D. Weighted ENO schemes for Hamilton–Jacobi equations. *SIAM Journal on Scientific Computing* 2000; **21**:2126–2143.
14. Jiang G-S, Shu CW. Efficient implementation of weighted ENO schemes. *Journal of Computational Physics* 1996; **126**:202–228.
15. Gottlieb S, Shu CW. Total variation diminishing Runge–Kutta schemes. *Mathematics of Computation* 1998; **67**:73–85.

